





RESEARCH ARTICLE | MARCH 01 2021

## Transient dynamics of soft particle glasses in startup shear flow. Part I: Microstructure and time scales

Fardin Khabaz  ; Bruno Flavio Di Dio; Michel Cloitre ; Roger T. Bonnecaze 

 Check for updates

*J. Rheol.* 65, 241–255 (2021)

<https://doi.org/10.1122/8.0000165>

 CHORUS



CrossMark



Advance your science, career  
and community as a member of  
**The Society of Rheology**

LEARN MORE





# Transient dynamics of soft particle glasses in startup shear flow. Part I: Microstructure and time scales

Fardin Khabaz,<sup>1,2,a)</sup> Bruno Flavio Di Dio,<sup>3</sup> Michel Cloitre,<sup>3</sup> and Roger T. Bonnecaze<sup>4</sup>

<sup>1</sup>*School of Polymer Science and Polymer Engineering, The University of Akron, Akron, Ohio, 78712*

<sup>2</sup>*Department of Chemical, Biomolecular, and Corrosion Engineering, The University of Akron, Akron, Ohio, 78712*

<sup>3</sup>*Molecular, Macromolecular Chemistry, and Materials, ESPCI Paris, CNRS, PSL University, 10 Rue Vauquelin, 75005 Paris, France*

<sup>4</sup>*McKetta Department of Chemical Engineering, The University of Texas at Austin, Austin, Texas, 78712*

(Received 17 September 2020; final revision received 27 December 2020; published 22 February 2021)

## Abstract

The rheology and microstructure of soft particle glasses during startup flow are studied using three-dimensional particle dynamics simulations at different particle volume fractions and shear rates. The behavior of transient stress depends on the applied shear rate. At high shear rates, soft particle glasses exhibit a static yield stress signaled by a stress overshoot followed by a relaxation to a steady-state value. The buildup of the stress is driven by an interplay between structural anisotropy due to an accumulation of particles along the compression axis and a depletion along the extension axis and a compression of particles that are soft and deformable. At low shear rates, the stress increase is monotonic and without any stress overshoot. The time scale at which structural anisotropy and the stress are maximum is correlated to the nonaffine dynamics of SPGs through the persistence time of shear-induced particle collisions and to the residence time of particles inside their transient cages. The static yield strain  $\gamma_p$  and the reduced static yield stress  $\sigma_p/\sigma_y$ , where  $\sigma_y$  is the dynamic yield stress deduced from steady flow measurements, follow universal behaviors when correlated with the dimensional shear rate  $\eta_s \dot{\gamma}/G_0$ , with  $\eta_s$  being the suspending fluid viscosity and  $G_0$  the storage modulus, which expresses the competition between elastic restoring forces and viscous dissipation. Dense suspensions of thermosensitive core-shell colloids, star-like micelles, and poly(ethylene oxide)-protected silica particles follow the same universal curves, suggesting the generality of our results. © 2021 The Society of Rheology. <https://doi.org/10.1122/8.0000165>

## I. INTRODUCTION

Glassy materials form a broad class of amorphous systems, which include colloidal [1] and metallic glasses [2], particulate gels [3], emulsions and foams [4], slurries and pastes [5], and soft particle glasses [6,7]. Despite the large diversity of their composition, they have in common many important features. At rest, they behave like amorphous solids that respond elastically to small perturbations. However, they can deform irreversibly and flow when they experience large enough stresses. This transition from solid to liquid with increasing stress is called “yielding.” Understanding and controlling the way that glassy materials yield and flow offer profound insights into the macroscopic rheology and microscopic dynamics of amorphous materials [8]. Furthermore, the question has essential applications in material science and engineering, such as drilling muds, high-performance coatings, food products, and ceramic pastes [9].

Startup flow experiments are familiar rheological techniques used to investigate the yielding properties of glassy materials. A startup flow experiment consists of applying a constant shear rate to the material initially at rest and monitoring the transient stress response. The stress first increases

linearly with the accumulated strain, which represents the elastic response of the material. At a larger strain, a more complex behavior takes over: the stress keeps on growing and eventually reaches a maximum value before decreasing to a steady-state value. The stress overshoot ( $\sigma_p$ ) represents the static yield stress or the minimum stress that the material has to overcome to start flowing. The position of the overshoot will be called “the static yield strain” ( $\gamma_p$ ) in the following. The static yield stress, the static yield strain, and the stress at steady state all depend on the applied shear rate. The static yield stress must not be confused with the dynamical yield stress ( $\sigma_y$ ), the minimum stress to maintain a steady flow. The dynamic yield stress corresponds to the low shear-rate limit of the steady flow curve  $\sigma(\dot{\gamma})$ , and it can be determined by fitting the flow curve to the Herschel-Bulkley equation  $\sigma = \sigma_y + k\dot{\gamma}^n$ . This phenomenology is quite general and has been reported in a variety of materials as different as colloidal glasses [10–22], metallic glasses [23–25], colloidal gels [26–36], nanocomposites [37], dense suspensions of soft particles [38–47], emulsions and foams [48–51], and polymer melts and solutions [52–57]. Transient yielding is vital for process design since the static yield stress can generate pressure perturbations during startup. It is also crucial from a fundamental perspective because it contains the evolution of the structure of the material from its initial state and reveals the microscopic mechanisms associated with relaxation to steady state. Different theories have attempted to

<sup>a)</sup>Author to whom correspondence should be addressed; electronic mail: [fkhabaz@uakron.edu](mailto:fkhabaz@uakron.edu)

capture the generic origin of stress overshoot in amorphous solids [58–60].

The yielding properties of hard-sphere suspensions in the entropic glass regime have been studied using a combination of experiments [9–18,21,22], molecular [10,13,16] and Brownian dynamics [12,13,19,20] simulations, and Mode-Coupling Theory (MCT) [10,12–19]. Three well-characterized model systems have been used at volume fractions between the glass transition and the close-packing volume fractions: sterically stabilized poly(methyl methacrylate) (PMMA) suspensions [10–13,15,16,19,21,22], core-shell particles consisting of a polystyrene core and crosslinked (*N*-isopropyl acrylamide) (PNIPAM) as the outer shell [14,15,18], and silica particles [17]. In hard-sphere suspensions, the transient response results from the competition between Brownian diffusion and flow advection which is expressed by the Peclet number ( $Pe$ ). In experiments and simulations, the normalized height of the overshoot is found to increase with the Peclet number and ranges from 0, i.e., the overshoot disappears when  $Pe \rightarrow 0$ , to about 0.5. In experiments, it is found that the stress overshoot decreases and even disappears when the volume fraction increases [12,19]. The static yield strain increases with the Peclet number from 0.1 to 0.4. MCT captures the shape of the stress response as well as the static yield stress and strain semiquantitatively [14,17,18].

The nonlinear stress response of hard-sphere glasses during startup flow is connected to the evolution of the microstructure, which has been investigated both in simulations [12,19,20] and in experiments using confocal microscopy [10,12,13,15,16,19] and x-ray scattering [17]. The application of shear flow distorts the particle distribution function in a way that particles accumulate along the compression axis and deplete along the extension axis. This local anisotropy is primarily responsible for the stress overshoot. It is maximum at the static yield strain and then decreases to a steady state as the stress accumulation is released [17]. The microscopic particle scale dynamics has been determined using confocal microscopy [10,12,13,16,19]. Plastic rearrangements are dominant after the stress overshoot [17]. Moreover, whereas particle motion is subdiffusive at rest because of cage effects, the dynamics becomes ballistic at an intermediate time scale during startup flow. Close to the glass transition volume fraction, the time scale of the stress overshoot has been correlated with the time scale of ballistic motion [10].

In the presence of attractive interactions, suspensions form attractive glasses at high volume fractions and gels at low volume fractions [3]. In attractive systems, yielding results from the competition between flow advection, bond dynamics, and Brownian motion. A two-step yielding with two distinct overshoots has been observed in experiments [28,29] and simulations [30–32]. The first step at strain values in the range of 0.01–0.1 is associated with the breaking of the attractive bonds: particles exchange neighbors, but they remain topologically trapped. The second step at much larger strain amplitudes corresponds to the opening of the cages, leading to the melting of the glass [11] or the fragmentation of the gel clusters [28,29,32]. Recent simulations have shown that this scenario may not be universal depending on the potential acting between colloidal particles in gels [36]. The transient

microstructure during startup shear flow of attractive gels is also characterized by strong anisotropy [32–34,36,55,61].

Besides hard particle suspensions, soft particle glasses (SPGs) constitute a broad class of materials, which are important for technological reasons and at the same time pose new fundamental questions. Unlike in hard-sphere suspensions, where particles interact only through excluded volume interactions, in SPGs, particles are jammed, and elastic contact forces make the dominant contribution to the microstructure and the rheology. Whereas hard particle suspensions have been widely studied, there exists far less systematic studies of the transient flow rheology of SPGs. Yet, startup flows of dense suspensions of thermosensitive microgels [40,44], polyethylene oxide-protected silica particles [38], multiarm star polymers [39], concentrated emulsions [48,49], dispersions of wax crystal in oil [45], and Carbopol suspensions [42] are characterized by a rich phenomenology including stress overshoots. The height of the peak usually increases with the time that the system has spent at rest after preshearing, but its location does not [38,39]. This feature, which is also present in hard-sphere glasses [22], has been attributed to aging. Still more intriguing, in some systems, stress overshoots are associated with a tendency to develop transient or permanent shear banding during yielding [39,42], a phenomenon that has been reproduced in simulations where particles interact through the Lennard-Jones potential [46,47].

In this paper, we analyze the connection between the existence of soft contact interactions and the transient behavior of soft particle glasses in startup shear flows from three perspectives: the scaling properties of the shear stress, the evolution of the microstructure from rest to a steady state, and the particle scale dynamics. We follow a micromechanical approach that was shown to successfully describe the steady-state rheology and the stress relaxation upon flow cessation of dense suspensions of microgels and concentrated emulsions [62–65]. Athermal particles interact through a soft Hertzian-like potential, which is relevant to real systems [6]. The micromechanical model is implemented in 3D large-scale simulations that provide the shear stress and normal stress differences growth as well as the transient evolution of the microstructure and the microscopic dynamics during startup flow. The stress growth proceeds through different stages, which are determined by an interplay between structural anisotropy and particle compression. The yield strain at which the peak overshoot is located and the value of the static yield stress are described by scaling laws explicitly accounting for particle elasticity and deformability. Our prediction compares well with available experimental data for dense suspensions of soft particles.

## II. MICROMECHANICAL MODEL AND SIMULATION METHOD

### A. Micromechanical model

The details of the model and the simulation method have been presented in previous studies [62–68] and, here, we review the important features. Soft particle glasses are modeled as suspensions of  $N$  non-Brownian elastic particles in a solvent with a viscosity  $\eta_s$ , which are jammed in a cubic simulation box at volume fractions larger than the random

close-packing of hard spheres. Suspensions with an average radius of unity, a polydispersity index of  $\delta = 0.2$ , and volume fractions of  $\phi = 0.7, 0.8$ , and  $0.9$  are studied. The value of the polydispersity agrees with that currently found in experiments [62,64]; it prevents crystallization at high shear rates [66,69]. Because the Poisson ratio for the particles is  $0.5$ , their volume remains constant upon deformation. The volume fraction of the suspension is computed as the ratio between the total volume of the particles and the volume of the box. As seen in Fig. 1(A), particles  $\alpha$  and  $\beta$  create a flat facet at contact, resulting in a deformation of  $\epsilon_{\alpha\beta} = 0.5(R_\alpha + R_\beta - r_{\alpha\beta})/R_c$ , where  $R_\alpha$  and  $R_\beta$  are the radii of particle  $\alpha$  and  $\beta$ ,  $r_{\alpha\beta}$  is the center-to-center distance, and  $R_c$  is the contact radius, which is given as  $R_c = R_\alpha R_\beta / (R_\alpha + R_\beta)$ . In the following,  $\epsilon_{\alpha\beta}$  is called the overlap deformation between particles  $\alpha$  and  $\beta$ .

Above the close-packing volume fraction, the particles are subjected to repulsive elastic forces that act perpendicularly to the contacting facets. The elastic force between two particles  $\alpha$  and  $\beta$  is given by the generalized Hertz law [62,63,70],

$$\mathbf{f}_{\alpha\beta}^e = \frac{4}{3} CE^* \epsilon_{\alpha\beta}^n R_c^2 \mathbf{n}_\perp, \quad (1)$$

where  $E^*$  is the particle contact modulus:  $E^* = E/2(1 - \nu^2)$ ,

with  $E$  being the Young modulus, and  $\nu$  is the Poisson ratio.  $C$  and  $n$  are parameters, which depend on the degree of compression. For  $\epsilon < 0.1$ ,  $n = 1.5$  and  $C = 1$ , for  $0.1 \leq \epsilon < 0.2$ ,  $n = 3$  and  $C = 32$ , and if  $0.2 \leq \epsilon < 0.6$ ,  $n = 5$  and  $C = 790$  [62,70].  $\mathbf{n}_\perp$  is the unit vector along the perpendicular direction to the facet. We also take into account elasto-hydrodynamic lubrication (EHD) forces, which are due to the flow of solvent in the thin films between the particles. The EHD force between the two particles is parallel to the contacting facets and is given by [62,63]

$$\mathbf{f}_{\alpha\beta}^{\text{EHD}} = -(\eta_s C u_{\alpha\beta,\parallel} E^* R_c^3)^{1/2} \epsilon_{\alpha\beta}^{(2n+1)/4} \mathbf{n}_\parallel, \quad (2)$$

where  $u_{\alpha\beta,\parallel}$  is the relative velocity component in the direction of  $\mathbf{n}_\parallel$ , which is the unit vector along the parallel direction to the facet. The fluid inertia is ignored, and the forces are assumed to be pairwise additive. The suspension is subjected to the velocity field  $\mathbf{u}_\alpha^\infty = \frac{\dot{\gamma} \eta_s}{E^*} y \mathbf{e}_x$ , where  $\mathbf{e}_x$  is the basis vector in the flow direction and  $y$  is the coordinate in the velocity gradient direction [see Fig. 1(B)]. The resulting equations of motion are made dimensionless by scaling lengths, time, and velocity by  $R$ ,  $\dot{\gamma}^{-1}$ , and  $\dot{\gamma} R$  respectively, leading to [62,63]

$$\frac{d\tilde{\mathbf{x}}_\alpha}{dt} = \tilde{\mathbf{u}}_\alpha^\infty + \frac{M}{R_\alpha} \left[ \frac{4}{3} C \tilde{\gamma}^{-1} \sum_\beta \epsilon_{\alpha\beta}^n \tilde{R}_c^2 \mathbf{n}_\perp - \tilde{\gamma}^{-1/2} \sum_\beta (C \tilde{u}_{\alpha\beta,\parallel} \tilde{R}_c^3)^{1/2} \epsilon_{\alpha\beta}^{(2n+1)/4} \mathbf{n}_\parallel \right], \quad (3)$$

where the tilde quantities are dimensionless variables,  $\mathbf{x}_\alpha$  is the position of particle  $\alpha$ , and  $M$  is the mobility function that belongs to a particle corrected by a factor  $f(\phi)$  that accounts for the reduction of mobility at a high volume fraction:  $M = f(\phi)/6\pi$ ;  $f(\phi)$  is set to  $0.08$  in the simulations to match the flow curves with experiments. The form of this equation shows that the dynamics is characterized solely by the dimensionless shear rate  $\tilde{\gamma} = \dot{\gamma} \eta_s / E^*$ , which represents the ratio of viscous to elastic forces, and the overlap deformation that depends on the volume fraction.

We have also determined the viscoelastic properties of SPGs using small amplitude shear rheology following our

previous works [69,71]. The suspensions are subjected in the  $x$  direction to an oscillatory shear strain of amplitude  $\gamma_0$  and frequency  $\omega$ :  $\gamma = \gamma_0 \sin \omega t$ . From the stress response, we can compute the storage modulus,  $G'(\omega)$ , and the loss modulus,  $G''(\omega)$ , as a function of frequency. The storage modulus exhibits a low-frequency plateau allowing the determination of the low-frequency modulus,  $G_0$ . We have also determined the low-frequency modulus of SPGs from the energy change computed during a cyclic uniaxial deformation [72]. Both methods lead to identical values of the low-frequency modulus.

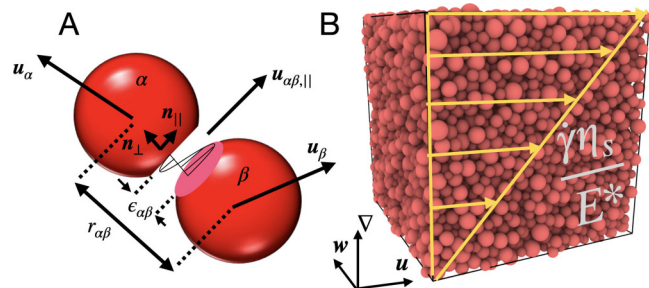


**FIG. 1.** (A) Schematic showing pairwise interaction between particles  $\alpha$  and  $\beta$ . (B) Configuration of a suspension with a volume fraction of  $0.9$  and a polydispersity index of  $\delta=0.2$ , which is subjected to shear flow. The flow ( $\mathbf{u}$ ), gradient ( $\nabla$ ), and vorticity ( $\mathbf{w}$ ) directions are labeled on the axes.

## B. Simulation method

A close-packed disordered structure is first created using the Lubachevsky and Stillinger algorithm [73] and compressed by reducing the box size until the desired volume fraction is achieved. The Lees–Edwards [74] boundary conditions are then used in the LAMMPS package [75] in order to impart the desired shear rate to the simulation box. The stress tensor of the suspensions is determined using the Kirkwood formula [76],

$$\boldsymbol{\sigma} = \frac{1}{V} \sum_\beta \sum_{\alpha>\beta} \mathbf{f}_{\alpha\beta}(\mathbf{x}_\alpha - \mathbf{x}_\beta), \quad (4)$$

where  $V$  is the volume of the system and  $\mathbf{f}_{\alpha\beta}$  is the total force acting on particle  $\alpha$  from particle  $\beta$ . The shear stress  $\sigma_{xy}$ , and the first and the second normal stress differences,  $N_1 = \sigma_{xx} - \sigma_{yy}$  and  $N_2 = \sigma_{yy} - \sigma_{zz}$ , are computed from the appropriate components of the stress tensor. The flow properties of the suspensions are investigated over a broad range of shear rates ranging from  $\dot{\gamma} = 10^{-9}$  to  $\dot{\gamma} = 10^{-4}$ . The simulations are performed for ten strain units, and the stress tensor is calculated at regular strain intervals. The value of the time step is chosen, such that it produces  $10^7$  steps per strain at each shear rate.

Equilibrium in this paper refers to mechanical equilibrium, where the net force on each particle is zero. SPG packings can be equilibrated during the initial preparation by using small compressive steps, allowing relaxation during each step using the conjugate gradient algorithm. We present two types of simulations: (i) startup flow simulations where a constant shear rate is applied to SPGs that are initially at rest and have been equilibrated (Secs. III A–III B) and (ii) startup simulations on SPGs that have been presheared and have not fully relaxed the residual forces on each particle and the resulting residual stresses accumulated during the preshear flow. In simulations of type (i), each particle is force- and torque-free, meaning particles in the suspension are in mechanical equilibrium and that there are no residual stresses. In measurements of type (ii), the startup flow takes place on a material that has been presheared and particles are not at mechanical equilibrium.

Most of the simulations are performed with  $10^4$  particles. At high shear rates ( $\dot{\gamma} > 10^{-7}$ ), we find that the stress–strain curves exhibit a clear stress overshoot and the results are independent of the simulation box size, simulations with  $1.25 \times 10^5$  and  $10^6$  particles leading to the same stress variations as simulations with  $10^4$  particles. At low shear rates ( $\dot{\gamma} \leq 10^{-7}$ ), the stress overshoot progressively decreases, and it is necessary to improve the accuracy of the calculations by increasing the number of particles in the simulation box. We perform simulations with  $10^3$ ,  $10^4$ ,  $1.25 \times 10^5$ , and  $10^6$  particles to investigate the effect of the number of particles on the

stress variations during startup flow at low shear rates, i.e., close to the yield point of the material. The shear stress as a function of the strain for two low values of the shear rate is plotted in Figs. 2(A) and 2(B). For  $10^3$  particles, the shear stress shows significant fluctuations, which make the detection of the overshoot challenging. As the number of particles increases up to  $10^6$ , the amplitude of the fluctuations is decreased, and a maximum in the stress becomes detectable. The standard deviation of the shear stress decreases when the number of particles increases as a power law [Fig. 2(C)]. A stress peak is detected when the difference between the maximum stress value and the steady-state stress is larger than the stress fluctuations.

The structural properties of the flowing suspensions are characterized by pair distribution functions. The dynamic pair distribution function  $g(\mathbf{r})$  in the flow gradient is computed at different strain values to investigate the structural rearrangement occurring during startup flow. To connect the microstructure to the macroscopic properties of the suspensions, the dynamic pair distribution function between the particles is decomposed into an orthogonal series of spherical harmonic functions [77],

$$g(\mathbf{r}) = g_0(r) + \sum_{l=1}^{\infty} \sum_{m=-l}^l g_{l,m}(r) Y_{l,m}(\theta, \phi), \quad (5)$$

where  $g_0(r)$  is the static pair distribution function. The functions  $Y_{lm}(\theta, \phi)$  are a set of orthogonal basis functions obtained from solutions of the Laplace equation in spherical coordinates [62].  $g_{l,m}(r)$  are the weighting function, which can be calculated as

$$g_{l,m}(r) = \frac{\int g(\mathbf{r}) Y_{l,m}(\theta, \phi) \sin(\phi) d\theta d\phi}{\int Y_{l,m}(\theta, \phi) Y_{l,m}(\theta, \phi) \sin(\phi) d\theta d\phi}. \quad (6)$$

The coefficient  $g_{2,-2}(r)$  of the expansion, which, here, is the dominant contribution to the shear component of the stress tensor [62], can be used to determine the elastic

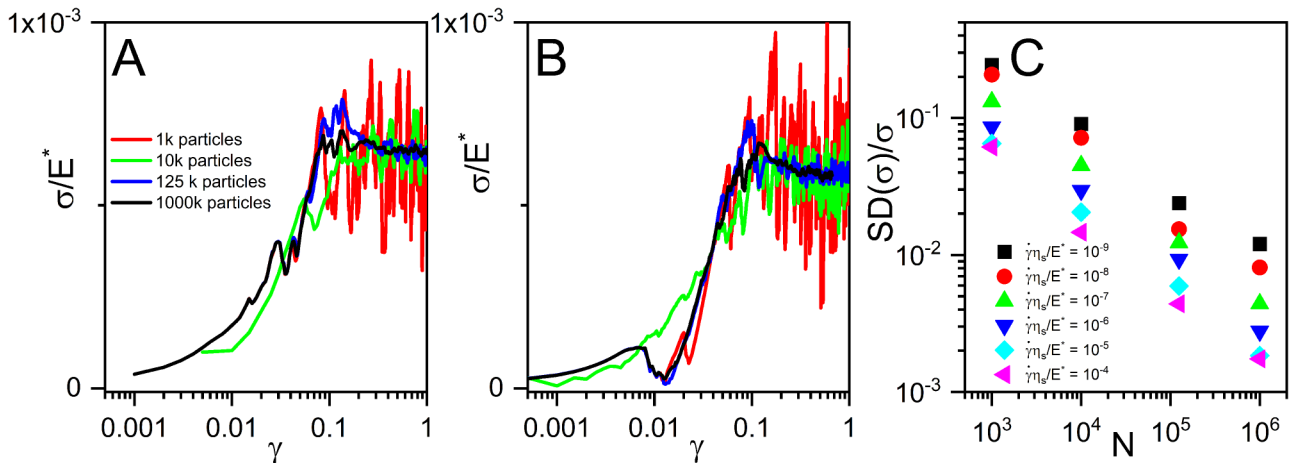


**FIG. 2.** Shear stress  $\sigma/E^*$  as a function of strain  $\gamma$  computed at (A)  $\dot{\gamma} = 10^{-8}$ , (B)  $\dot{\gamma} = 10^{-9}$  for suspensions with different numbers of particles. (C) The standard deviation (SD) of the shear stress normalized with respect to the steady-state stress at different shear rates as a function of the number of particles. The volume fraction is  $\phi = 0.8$ .



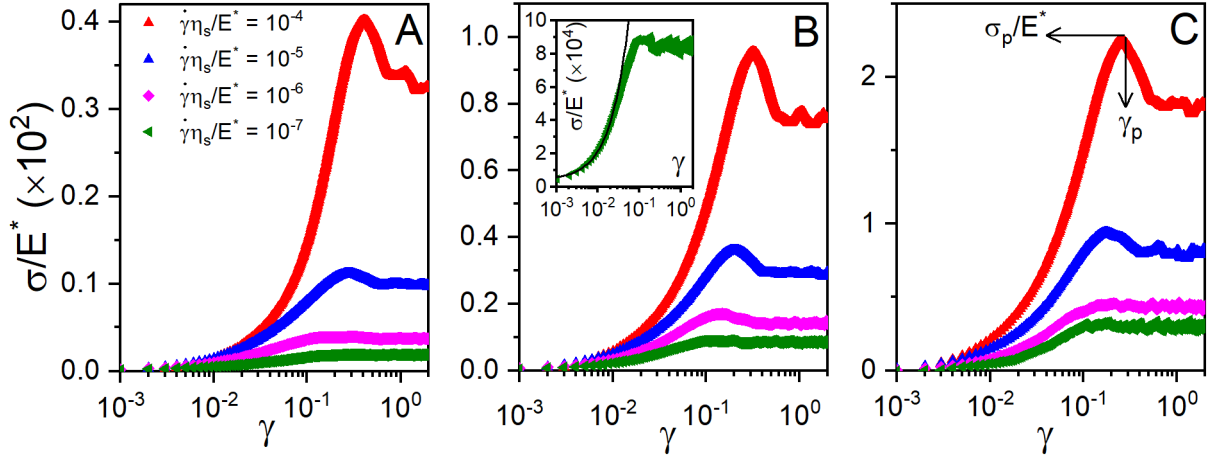


**FIG. 3.** Shear stress  $\sigma/E^*$  as a function of  $\gamma$  obtained at different shear rates and volume fractions of (A)  $\phi = 0.7$ , (B)  $\phi = 0.8$ , and (C)  $\phi = 0.9$ . The inset in (B) shows that for  $\dot{\gamma}\eta_s/E^* = 10^{-7}$ , the stress at small strain compares well with the elastic response based on the low-frequency modulus. The color coding in (B) and (C) is the same as in (A).

contribution to the shear stress,

$$\sigma = -n^2 \sqrt{\frac{\pi}{15}} \int_0^{2R} r^3 f^e(r) g_{2,-2}(r) dr, \quad (7)$$

where  $n$  is the number density of particles and  $f^e(r)$  is the elastic force between particle pairs.

We have connected the macroscopic rheology during startup flow to the nonaffine microscopic dynamics of SPGs under shear, focusing on the persistence time of shear-induced particle collisions and on the residence time that characterizes the time particles spend in their cages before hopping to another environment [68]. The persistence time is obtained from the normalized autocorrelation function of the contact elastic force experienced by the particles when they collide,

$$C(t) = \left\langle \frac{\mathbf{F}(t + t_0) \cdot \mathbf{F}(t_0)}{|\mathbf{F}(t_0)|^2} \right\rangle, \quad (8)$$

where  $\mathbf{F}(t)$  is the elastic force on a particle at time  $t$  and  $|\mathbf{F}(t_0)|$  the magnitude of the force fluctuations. Correlation functions  $C(t)$  have been computed for different shear rates and different volume fractions, and for each of them, the persistence time  $t_d$  has been determined from the decay time defined as  $C(t_d) = 1/e$ . The residence time has been obtained from the incoherent scattering function,

$$F_s(\mathbf{k}, t) = \frac{1}{N} \left\langle \sum_{j=1}^N \exp[i\mathbf{k} \cdot (\mathbf{r}_j(t) - \mathbf{r}_j(0))] \right\rangle, \quad (9)$$

where  $\mathbf{k}$  is a spatial wave vector and  $N$  is the total number of the particles in the simulation. We have calculated the incoherent scattering function at different volume fractions and shear rates at a wave vector  $kR = 4.0$ , which corresponds to the cage size. The time decay of the incoherent scattering function is almost exponential, from which we determine the residence  $t_c$ . When  $t_d$  and  $t_c$  are nondimensionalized using the

shear rate, we get the so-called persistence strain  $\gamma_d$  and the residence strain  $\gamma_d$  that can be compared to the static yield strain. The reader is referred to our recent study [68] for more details on the calculations and discussion on the importance of these two quantities in determining the macroscopic rheology of SPGs.

### III. RESULTS

#### A. Macroscopic properties' evolution during startup flow

The shear stress ( $\sigma/E^*$ ) as a function of the shear strain ( $\gamma$ ) is plotted in Figs. 3(A)–3(C) for suspensions with volume fractions of  $\phi = 0.7$ , 0.8, and 0.9 in simulations at different shear rates ranging from  $\dot{\gamma} = 10^{-9}$  to  $\dot{\gamma} = 10^{-4}$ . Switching the shear flow on from rest, the shear stress ( $\sigma/E^*$ ) initially exhibits a nearly linear increase corresponding to the elastic response of the SPG followed by a nonlinear behavior. The shear stress undergoes an overshoot, and by releasing the stored stress, it decreases and reaches a steady state. At lower shear rates, the overshoot disappears at large volume fractions. This observation reveals that yielding is smooth and monotonic at low shear rates, but it is characterized by stress overshoots at high enough shear rates. A stress overshoot represents the minimum stress to apply in order to initiate macroscopic flow and it corresponds to the static yield point. This behavior occurs consistently for all volume fractions at high enough shear rates. The first ( $N_1/E^*$ ) and the second normal ( $-N_2/E^*$ ) stress differences exhibit similar variations (see supplementary material S1 [78]).

In the following, we characterize the static yield point by the position and the value of the stress overshoot,  $\gamma_p$  and  $\sigma_p$  respectively, when it exists. The variations of  $\gamma_p$  as a function of the shear rate  $\dot{\gamma}$  are plotted in Fig. 4(A).  $\gamma_p$  takes a value close to 0.1 at low shear rates and increases with the applied shear rate up to a value of 0.45. In addition, increasing the volume fraction of the suspensions at a given shear rate leads to a decrease in the value of  $\gamma_p$ . The values of  $\sigma_p/E^*$  are plotted as a function of  $\dot{\gamma}$  in Fig. 4(B). They are well fitted

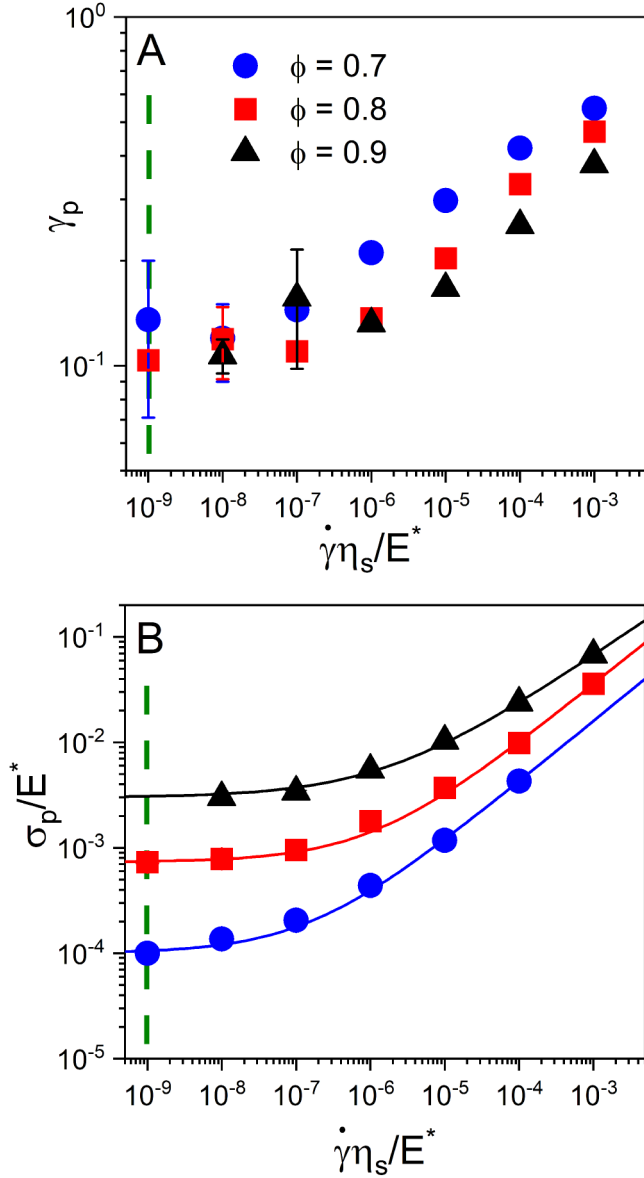


**FIG. 4.** (A) Strain  $\gamma_p$ , at which the shear stress shows a maximum (static yield strain) and (B) peak stress  $\sigma_p/E^*$  (static yield stress) as a function of shear rate  $\dot{\gamma} = \eta_s \dot{\gamma}/E^*$  for the three volume fractions investigated. The green dashed line shows the lowest shear rate that above  $\dot{\gamma} = 10^{-9}$  simulations can detect a stress overshoot.

to the Herschel–Bulkley (HB) equation:  $\sigma_p/E^* = (\sigma_p/E^*)_y + k(\dot{\gamma}\eta_s/E^*)^n$ , where  $(\sigma_p/E^*)_y$  is the value of the stress overshoot at the lower limit of shear rates shown by the dashed green line in these two figures. The values of the fitting parameters are reported in Table I. We note that the value of the exponent decreases from 0.58 to 0.48 when the volume fraction increases from 0.7 to 0.9.

**TABLE I.** Fit parameters of the HB equation for the stress overshoot values in SPGs with different volume fractions.

$\phi$	$(\sigma_p/E^*)_y$	$k$	$n$
0.70	0.00010	0.856	0.58
0.80	0.00073	1.809	0.57
0.90	0.00300	1.862	0.49

## B. Microstructure distortions during startup flow

The local microstructure of the suspension exhibits extreme changes during startup flow. Examining these changes provides valuable information about the physical mechanisms associated with yielding. We discuss the high and low shear rates cases separately.

### 1. Dynamic microstructure for high applied shear rates

When the applied shear rate is large, the transient stress is characterized by the existence of a static yield stress. Figures 5(A)–5(E) show two-dimensional pair correlation functions  $g(\mathbf{r})$  in the flow-gradient plane computed at different strains for an applied shear rate of  $\dot{\gamma} = 10^{-4}$  at a volume fraction of  $\phi = 0.8$ . For a guide to the reader, the shear stress as a function strain curve is plotted in Fig. 5(F). At rest, the suspension is at equilibrium, and the contacts between the reference and the test particles are uniformly distributed. Note that the particles are soft, and the interparticle distance is smaller than twice the nominal radius of these particles. As the strain increases (around  $\gamma = 0.1$ ), we observe an accumulation of particles along the upstream compressive quadrant. In contrast, a depletion of particles is seen along the extension axis [Fig. 6(A)]. The anisotropy increases with the strain [Fig. 5(B)] and becomes maximum at the strain  $\gamma_p$  where the stress overshoot takes place [Fig. 5(C)]. After the overshoot, the anisotropy decreases, and concomitantly the stress is relaxed and reaches a steady state. This is evident by comparing the pair correlation functions in Figs. 5(B) and 5(D), corresponding to points B and D in Fig. 5(F), which have the same stress values but different locations on the stress–strain curve. In supplementary material S2 [78], we show the pair distribution functions of the suspensions at steady state when the shear rate is varied from  $10^{-9}$  to  $10^{-4}$ . The significant anisotropy that persists at steady state is central to the nonlinear rheology of SPGs [62].

To capture the distortions of the pair correlation function in a more quantitative way, we expand  $g(r)$  in spherical harmonics, and we compute the coefficient  $g_{2,-2}(r)$  at different strains, as explained in Sec. II [Fig. 5(E)].  $g_{2,-2}(r)$  gives access to the shear stress. Other components that are relevant to the normal stress differences are presented and discussed in supplementary material S3 [78]. Initially, at rest,  $g_{2,-2}(r)$  is close to zero with some minor fluctuations (data not shown). As the strain increases to  $\gamma = 0.1$  [point A in the stress–strain curve in Fig. 5(F)], a negative minimum and a positive maximum appear. The negative minimum corresponds to the accumulation of particles around the compression axis, whereas the positive maximum is associated with the depletion of particles around the extension axis. The minimum is located at a distance  $r_m = 1.85R$  that is only slightly smaller than the center-to-center distance  $r_m = 1.88R$  between particles at rest, and the maximum is seen at larger  $r$  values. Increasing the strain to  $\gamma = 0.2$  [point B in Fig. 5(F)] essentially changes the values of the maximum and the minimum, revealing a slight decrease of anisotropy, whereas their positions are not much affected. At the overshoot  $\gamma_p = 0.32$  [point C in Fig. 5(F)], the position of the minimum shifts to a smaller distance, i.e., particles are more compressed, and the magnitudes

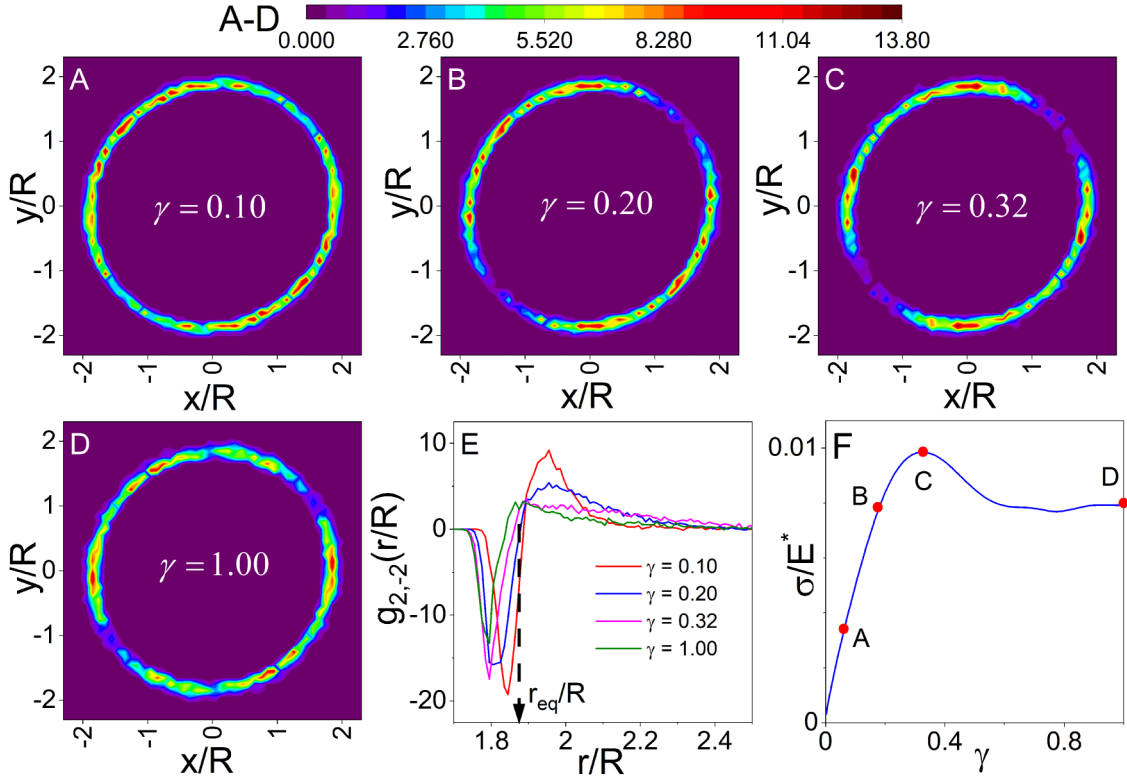


**FIG. 5.** (A-D) Two-dimensional pair distribution function  $g(\mathbf{r})$  obtained at different strains, (E) spherical harmonics coefficient  $g_{2,-2}(r/R)$  at different strains corresponding to (A-D), and (F) shear stress  $\sigma/E^*$  as a function of the strain. The equilibrium center-to-center distance between particles (denoted by the dashed arrow) is determined from the peak of the pair distribution function at rest. The volume fraction is  $\phi = 0.8$ , and the shear rate is  $\dot{\gamma} = \eta_s \dot{\gamma}/E^* = 10^{-4}$ . The data are obtained with  $10^4$  particles.

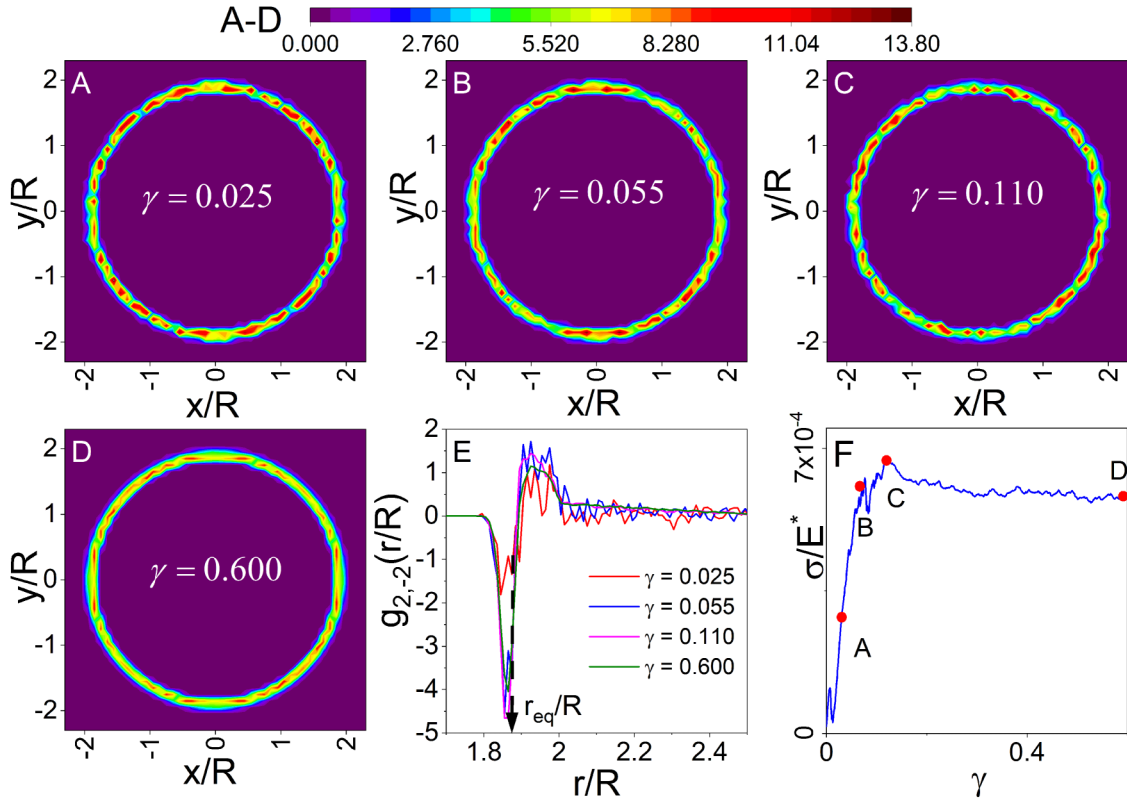


**FIG. 6.** (A-D) Two-dimensional pair distribution function  $g(\mathbf{r})$  obtained at different strains, (E) spherical harmonics coefficient  $g_{2,-2}(r/R)$  at different strains corresponding to (A-D), and (F) shear stress  $\sigma/E^*$  as a function of the strain. The equilibrium contact distance between particles (denoted by the dashed arrow) is determined from the peak of the pair distribution function at rest. The volume fraction is  $\phi = 0.8$ , and the shear rate is  $\dot{\gamma} = \eta_s \dot{\gamma}/E^* = 10^{-9}$ . The data are obtained with  $10^6$  particles.



of the maximum and the minimum corresponding to accumulation and depletion, i.e., the anisotropy, decrease. An increase in the strain up to steady state [point D in Fig. 5(F)] leads to a further decrease in the magnitude of the minimum and the maximum. These results show that the microstructural changes during startup flow at high shear rates result from an interplay between anisotropy due to the accumulation–depletion of contacts and compression. The static yield stress appears to be the point where the anisotropy is maximum before being relaxed as the particle contacts are redistributed.

## 2. Dynamic microstructure at low applied shear rates

When the applied shear rate is low, the static yield stress is weak, and the stress buildup is monotonic. The two-dimensional pair correlation functions in the flow–gradient plane for different strain values when a shear rate of  $\dot{\gamma} = 10^{-9}$  is applied are shown in Figs. 6(A)–6(E). The computations now use a box containing  $10^6$  particles. At low strain values, the contacts are isotropically distributed around the reference particle [Fig. 6(A)], while shearing the SPGs leads to anisotropy as above, although it is weaker than at high shear rates, reflecting the fact that the stress amplitude is much smaller [Fig. 6(B)]. Again, the anisotropy is maximum at the stress overshoot [Fig. 6(C)] and decreases as a steady state is approached [Fig. 6(D)]. The variations of the  $g_{2,-2}(r)$  coefficient are shown

in Fig. 7(E). As before,  $g_{2,-2}(r)$  exhibits a negative minimum and a positive maximum whose absolute magnitude steadily decreases as the strain is increased. The position of the peaks does not vary significantly, indicating that compression is much weaker than at high shear rates. This further confirms that the existence of the static yield stress results from the interplay between anisotropy and compression. Furthermore, we also observe that the fluctuations in  $g_{2,-2}(r)$  decrease substantially when the shear flow reaches its steady-state value.

## 3. Contact number and particle overlap

To further investigate microstructure changes during yielding, we have computed the number of contacts  $N_c$ , overlap deformation  $\varepsilon$  per particle, and the elastic energy as a function of the strain at different shear rates. To determine  $N_c$ , we consider that two particles are in contact if the center-to-center distance is less than the sum of their radii. The results for  $\phi = 0.8$  are presented in supplementary material S4 [82]. Both the number of contacts and the overlap deformation of the SPGs follow normal distributions [see Figs. S4(A)–S4(D) in the supplementary material [78]]. The contact number distributions are broad with a standard deviation of about 2.0. At a low shear rate, the standard deviation is equal to 2.35 and is independent of the strain. The same trend is observed for the overlap distribution functions [see

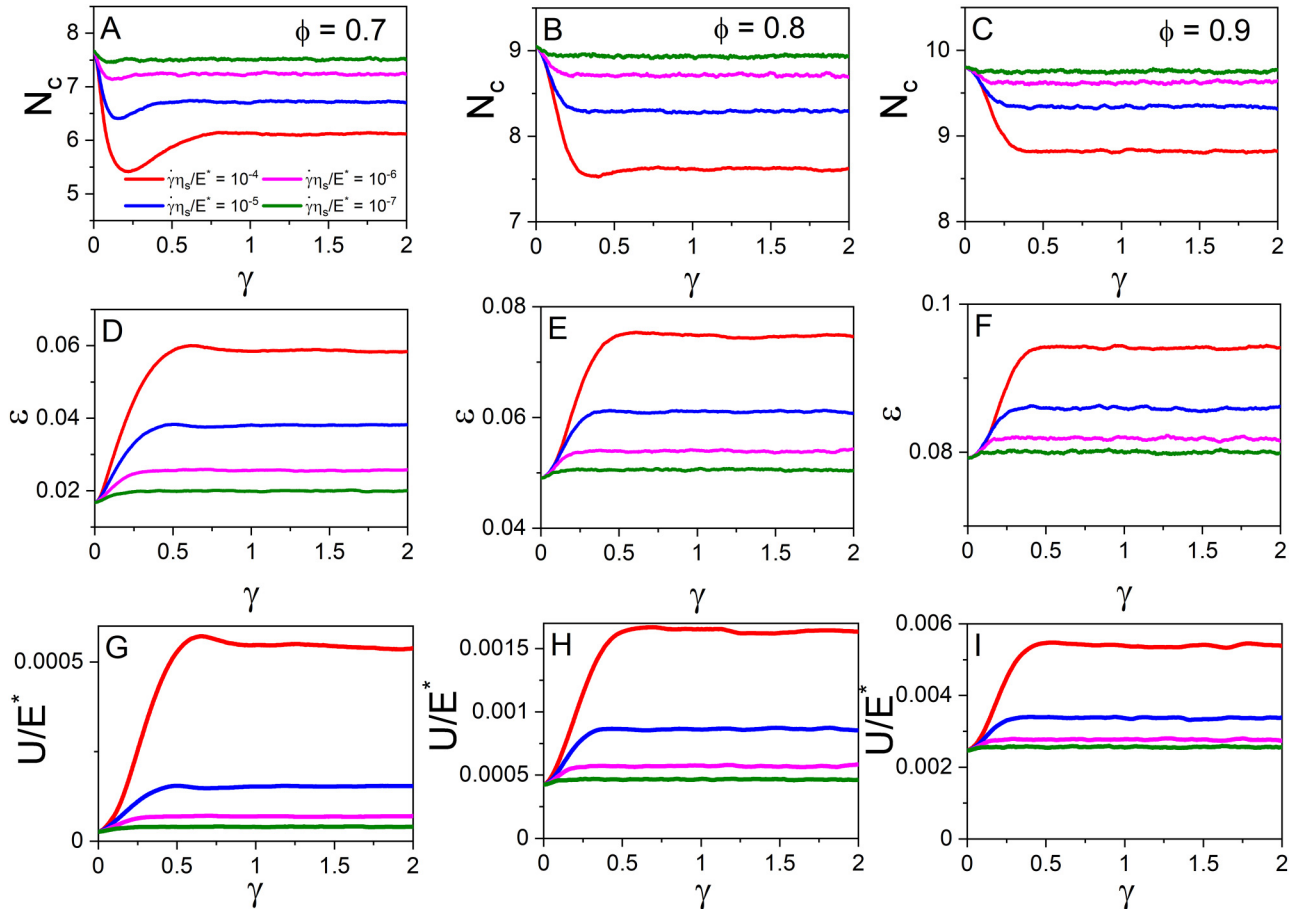


**FIG. 7.** Evolution of (A–C) the average number of contacts  $N_c$ , (D–F) the average overlap deformation  $\varepsilon$  per particle, and (G–I) the elastic energy scaled with the volume  $U/E^*$  as a function of  $\gamma$  at different volume fractions of  $\phi = 0.7$ ,  $\phi = 0.8$ , and  $\phi = 0.9$ . The statistical distributions of the overlap parameter and contacts at different strains for low and high shear rates are presented in Figs. S4(A)–S4(D) [78].

Figs. S4(C)–S4(D) [78]. They are broad with a standard deviation of about 0.02. At large shear rates, the distributions become wider when the strain increases. At low shear rates, the standard deviation of the distribution is about 0.018 independent of the strain value.

The average number of contacts,  $N_c$ , is represented as a function of the strain  $\gamma$  in Figs. 7(A)–7(C) for  $\phi = 0.7, 0.8$ , and 0.9. At the lowest volume fraction  $\phi = 0.70$  [Fig. 7(A)], when the applied shear rate is large ( $\dot{\gamma} = 10^{-4}$ ),  $N_c$  shows a minimum at the yield strain  $\gamma_p$  where the stress is maximum and then reaches a steady-state value. When the shear rate decreases, the number of contacts increases, and the minimum becomes shallower. Increasing the volume fraction leads to a weaker minimum and a larger number of contacts per particle [Figs. 7(B)–7(C)]. These results show that the accumulation–depletion mechanism leads to a decrease in the average contact number  $N_c$ .

Let us now turn our attention to the variations of the average overlap deformation per particle,  $\varepsilon$ , as a function of strain  $\gamma$  [Figs. 7(D)–7(F)]. At high shear rates,  $\varepsilon$  exhibits a weak overshoot before decreasing to its steady-state value. The overshoot disappears as the shear rate decreases, and it is weaker when the volume fraction increases. Interestingly, the overshoot occurs for a strain larger than  $\gamma_p$ , supporting our previous finding that the compression of the particles, which increases the overlap distance, is linked to particle redistribution and ultimately to the relaxation of the stress to its final value.

Finally, the elastic energy per particle is shown as a function of the strain  $\gamma$  in Figs. 7(G)–7(I). Given that the elastic energy is a function of the average number of contacts and of the average overlap, it also exhibits an almost monotonic behavior with very weak overshoots compared with those seen in the shear stress and the normal stress differences as a function of  $\gamma$  in Figs. 3 and supplementary material S1 [78], respectively.

### C. Effect of mechanical history on start flow properties

The results presented so far are computed starting from fully equilibrated suspensions where each particle is at rest and subjected to a net-zero force. This situation is rarely encountered in experiments where suspensions experience a

complex mechanical history, the effect of which slowly relax in the course of time. Two important phenomena have been reported in this respect: the capacity of SPGs to store residual stresses [64,65] and physical aging [38,79]. In order to start from a reproducible mechanical state, SPGs are usually presheared above the yield point and kept at rest for the so-called waiting time,  $t_w$ , before any further measurement. We reproduce the same protocol in our simulations by preshearing SPGs at different volume fractions ( $\phi = 0.7, 0.8$ , and 0.9) at a rate of  $\dot{\gamma} = 10^{-6}$ , switching off the preshear flow for different waiting periods ( $t_w E^*/\eta_s = 2 \times 10^6 - 2 \times 10^8$ ), and finally turning on the shear flow. Here, we present results for the shear rate  $\dot{\gamma} = 10^{-6}$ , which corresponds to a shear rate value commonly used in experiments [64]. The evolution of shear stress is shown in Figs. 8(A)–8(C). For all volume fractions, the shear stress shows an overshoot just as found in the previous section, but now both the magnitude and the location of the overshoot depend on the waiting time. The peak magnitude, i.e., the static yield stress, increases with the waiting time. In the literature, this observation has been attributed to aging [22,38,39]. At short waiting times, the location of the stress overshoot, i.e., the static yield strain, is slightly shifted to smaller strains, but later on, it increases and approaches to that for relaxed configurations (i.e.,  $t_w E^*/\eta_s = \infty$ ). Furthermore, the initial response of the stress is shifted upward compared with the data obtained from the relaxed structure. This stress increase represents the contribution of the residual stress stored inside the suspension during the preshear flow, which has not relaxed during the waiting period. The same behavior is found when the SPGs are sheared at high shear rates (see supplementary material S5 [78]).

We now analyze these results from a microstructural perspective using the variations of the coefficient  $g_{2,-2}(r)$  already used earlier. Figure 9(A) represents the variations of  $g_{2,-2}(r)$  at the end of the waiting period for different values of the waiting time. When the waiting time is short,  $g_{2,-2}(r)$  has a negative minimum and a small positive maximum, confirming that the accumulation–depletion anisotropy created during preshear persists over the waiting period. This anisotropy is responsible for the residual stress detected in the startup flow response. As the waiting time becomes longer,  $g_{2,-2}(r)$  fluctuates around zero and its minimum becomes smaller, expressing the gradual

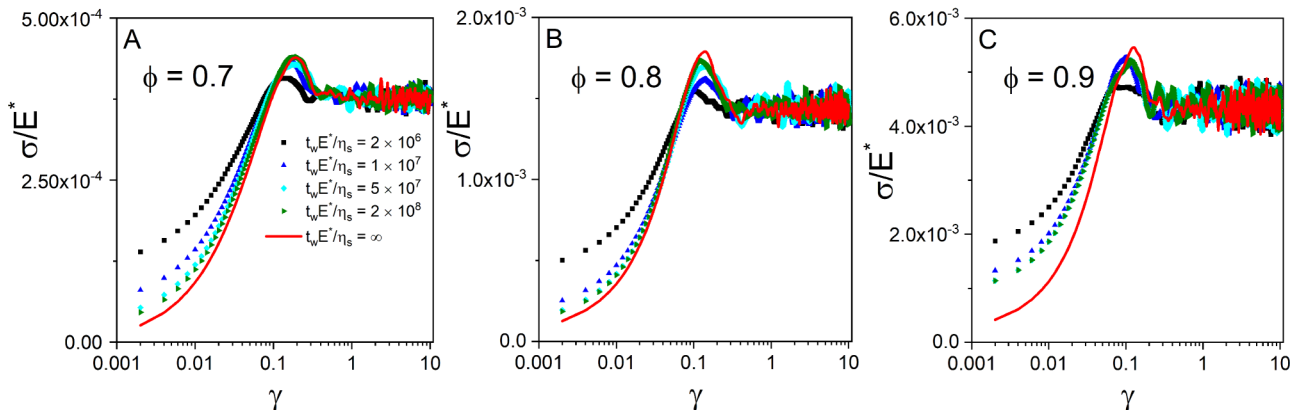


**FIG. 8.** Shear stress as a function of strain in SPGs aged over different waiting times. The volume fractions are: (A)  $\phi = 0.7$ , (B)  $\phi = 0.8$ , and (C)  $\phi = 0.9$ ; the applied shear rate is  $\dot{\gamma} = \eta_s \dot{\gamma}^*/E^* = 10^{-6}$ .

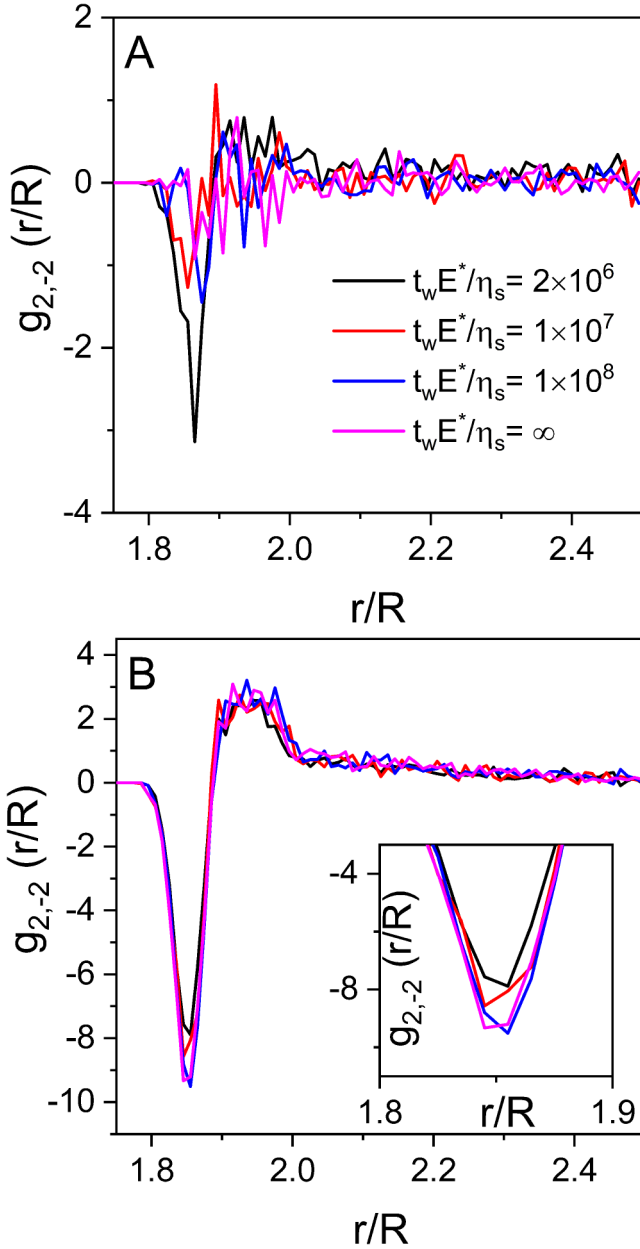


FIG. 9. Spherical harmonics coefficient  $g_{2,-2}(r)$  (A) at the end of the waiting time after preshearing the SPGs (B) at the stress overshoot obtained at different waiting times. The volume fraction is  $\phi = 0.8$ , and the shear rate is  $\dot{\gamma} = \eta_s \dot{\gamma} / E^* = 10^{-6}$ .

relaxation of the residual stress. Figure 9(B) represents the variations of  $g_{2,-2}(r)$  during startup flow ( $\dot{\gamma} = 10^{-6}$ ) for a strain  $\gamma_p$  corresponding to the location of the overshoot.  $g_{2,-2}(r)$  shows a negative minimum and a positive maximum as expected. However, the depth of the minimum of  $g_{2,-2}(r)$  is monotonically correlated with the age of the SPG, as seen in the inset of Fig. 9(B).

## IV. DISCUSSION

### A. Scaling properties of the static yield strain and static yield stress

In this section, we show that the dimensionless shear rate  $\hat{\gamma} = \dot{\gamma} \eta_s / G_0$ , where  $G_0$  is the low-frequency modulus and  $\eta_s$  the solvent viscosity, is the relevant variable that controls the

values of the static yield strain  $\gamma_p$  and the static yield stress  $\sigma_p$  shown in Fig. 4. The low-frequency modulus is determined from Small Amplitude Oscillatory Shear Rheology computations, as described in Sec. II. The dimensional shear rate  $\dot{\gamma} = \dot{\gamma} \eta_s / G_0$  characterizes the competition between the advection time  $\dot{\gamma}^{-1}$  and the local relaxation time  $\eta_s / G_0$ . It was first introduced to unify the flow properties of SPGs [6,63,80] and recently extended to rationalize their particle scale dynamical properties [68]. Figure 10(A) shows that this variable successfully collapses the static yield strain values  $\gamma_p$  computed over a broad range of shear rates for different volume fractions. The master curve follows the power-law variation  $\gamma_p \sim \hat{\gamma}^{0.30 \pm 0.05}$  at high shear rates and tends to the limit 0.1 at low shear rates; it is well described by the Herschel–Bulkley relationship of the form:  $\gamma_p = 0.1(\pm 0.02) + 1.00(\pm 0.12)\hat{\gamma}^{0.3(\pm 0.05)}$ . Power-law relationships have also been found for the static yield strain  $\gamma_p$  of polymer melts [55,81] [ $\gamma_p \simeq (\dot{\gamma} \tau_R)^{1/3}$  for  $\dot{\gamma} \tau_R > 1$ , where  $\tau_R$  is the Rouse relaxation time of the chain, and  $\gamma_p \simeq (\dot{\gamma} \tau_R)^{1/5}$  for  $\dot{\gamma} \tau_R < 1$ ] as well as for carbon nanotubes/poly(ethylene oxide) composites [82] where  $\gamma_p \simeq \dot{\gamma}^{1/4}$ . In polymeric materials, stress overshoots have a different physical origin, i.e., the segmental orientation of chains in shear flow, which is fundamentally different from the accumulation–depletion mechanism at work in SPGs. Figure 10(B) shows the values of the static yield stress  $\sigma_p$  normalized by the dynamical yield stress  $\sigma_y$  plotted against  $\hat{\gamma}$ . The values of  $\sigma_y$  are obtained from the extrapolation of the flow curves to zero shear rate (see supplementary material S6 [78]). This combination of variables successfully collapses the data computed for different volume fractions. Another important result here is that the stress overshoot  $\sigma_p$  scales with the dynamical yield stress  $\sigma_y$ . The value of  $\sigma_p / \sigma_y$  increases from a value just above unity and follows an HB relationship according to  $\sigma_p / \sigma_y = 1.2(\pm 0.3) + 350(\pm 25)\hat{\gamma}^{0.55(\pm 0.1)}$ , which is very close to the HB variations describing the flow curves of these materials [63]. At very low shear rates, the fact that  $\sigma_p / \sigma_y$  tends to unity indicates that there is no stress overshoot and that yielding is monotonic without any static yield stress.

### B. Comparison with experiments

In the literature there exists a few sets of data that are available for comparison with our predictions. We have revisited results obtained for dense suspensions of thermosensitive colloids consisting of a polystyrene core covered with a shell of crosslinked poly(*N*-isopropylacrylamide) [40,43], star-like micelles [43], and poly(ethylene oxide)-protected silica particles [38]. All these systems can be viewed as being SPGs where particles are in contact. We have also used data obtained for entropic glasses of core-shell polystyrene/ poly(*N*-isopropylacrylamide) colloids [14,18]. The static yield strain  $\gamma_p$  and the reduced static yield stress  $\sigma_p / \sigma$  extracted for these different systems from [14,18,38,40,43] are plotted against the reduced shear rate  $\hat{\gamma} = \dot{\gamma} \eta_s / G_0$  in Figs. 11(A)–11(B), respectively. Details about the data reduction method are given in supplementary material S7 [78]. It is important to note that the data replotted from the literature may be affected by significant uncertainties due to unspecified inertia effects at high shear rates, short waiting times, and other

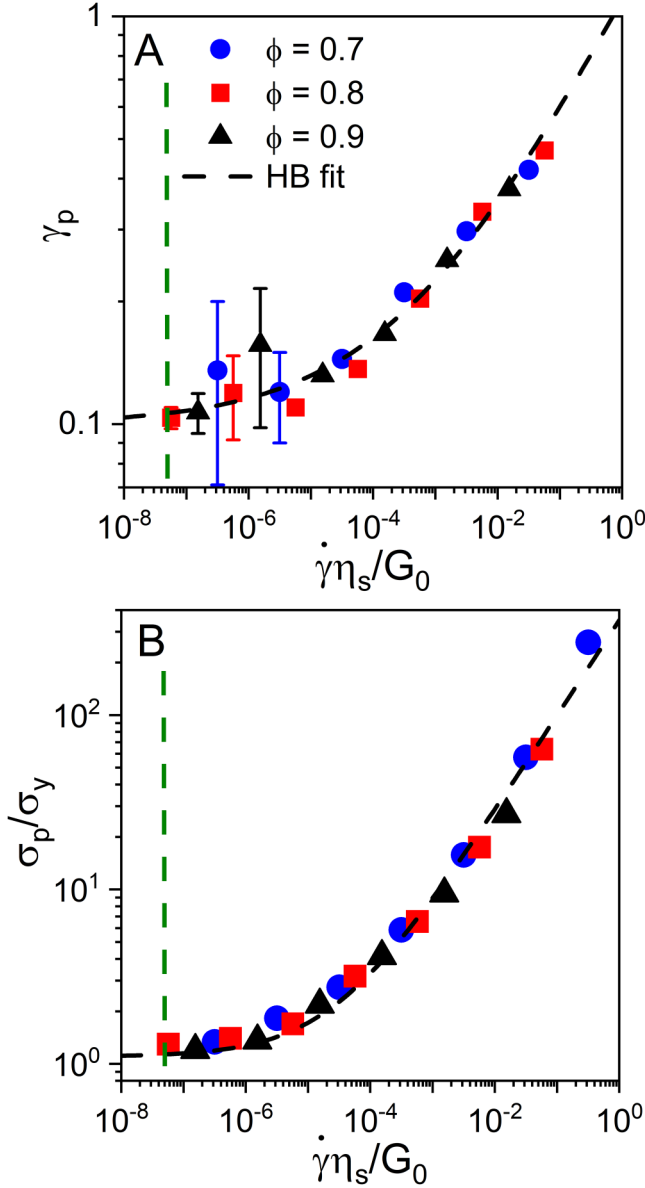


**FIG. 10.** Master curves of (A)  $\gamma_p$  and (B) the rescaled stress overshoot  $\sigma_p/\sigma_y$  as a function of the reduced shear rate  $\dot{\gamma} = \dot{\gamma}\eta_s/G_0$ . The HB fits for  $\gamma_p$  and  $\sigma_p/\sigma_y$  are given by:  $\gamma_p = 0.1(\pm 0.02) + 1.00(\pm 0.12)\dot{\gamma}^{0.3(\pm 0.05)}$  and  $\sigma_p/\sigma_y = 1.2(\pm 0.3) + 350(\pm 25)\dot{\gamma}^{0.55(\pm 0.1)}$ , respectively. The green dashed line shows the lowest shear rate above which simulations can detect a stress overshoot.

experimental issues. Both the static yield strain  $\gamma_p$  and the reduced static yield stress  $\sigma_p/\sigma_y$  agree reasonably well with the simulation predictions, although they do not perfectly collapse onto the master curves. For the static yield strain  $\gamma_p$ , the discrepancies are the highest at high shear rates where inertia contributions become critical. It is interesting to note that the values of the static yield strain and the static yield stress of hard-sphere glasses closely match our predictions, although their rheology obeys physics different from that of SPGs.

### C. Connection with particle scale dynamical properties

In a recent paper, using our particle dynamics simulations, we have shown that the macroscopic flow properties of SPGs

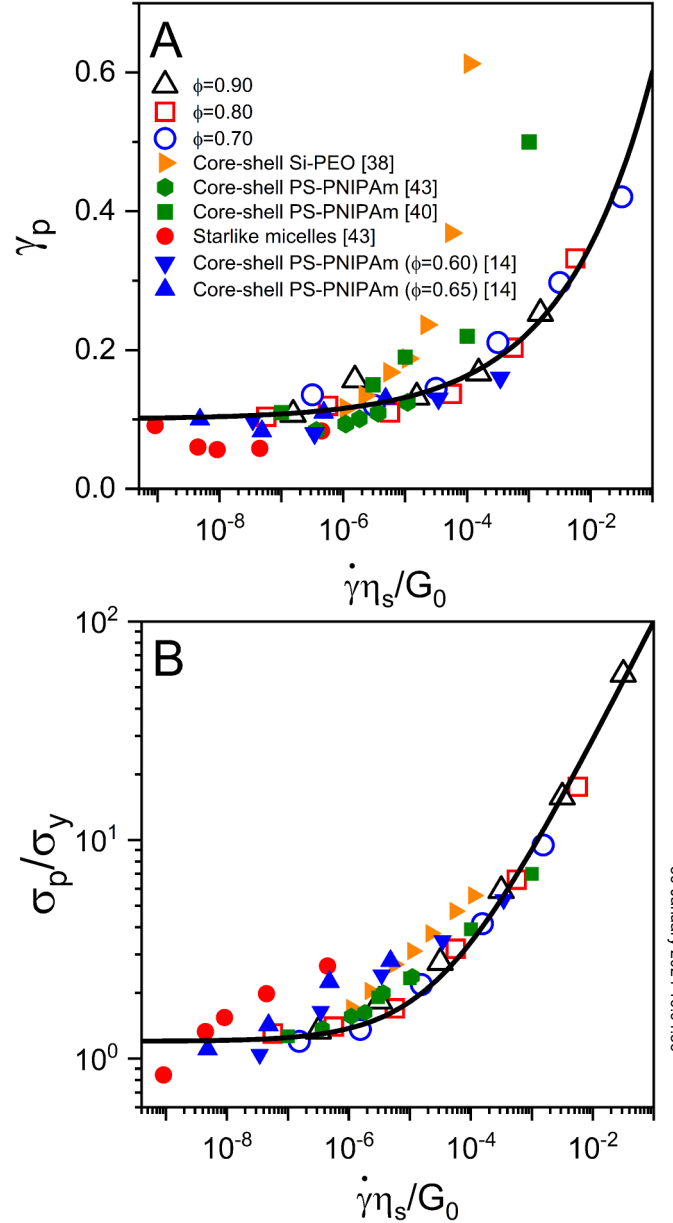


**FIG. 11.** Comparison of simulations and experimental data: master curves of (A)  $\gamma_p$  and (B) rescaled stress overshoot  $\sigma_p/\sigma_y$  as a function of the reduced shear rate  $\dot{\gamma} = \dot{\gamma}\eta_s/G_0$ . Simulation results are shown with open symbols.

are intimately related to their nonaffine microscopic dynamics [68]. At very short times, particles rattle in the cages formed by their neighbors against which they collide and rebound elastically. Particles move locally in their cages during the residence time  $t_c$  (or equivalently the residence strain  $\gamma_c = \dot{\gamma}t_c$ ) after which they hop on another position. At smaller time scales, the persistence time  $t_d$  (or equivalently, the persistence strain  $\gamma_d = \dot{\gamma}t_d$ ) of the net elastic force experienced by the particles during collisions constitutes the elementary clock that controls the entire sequence of dynamical processes taking place in SPGs. The determination of  $\gamma_d$  and  $\gamma_c$  is described in Sec. II. The reader is also referred to our recent study [68] for details of calculations and a discussion on the importance of these two time scales in determining the macroscopic rheology of SPGs. Coming back to the



startup flow problem, the stress response at a small strain is controlled by the SPG elasticity so that particle displacements must be extremely localized. However, close to the stress overshoot, particle scale rearrangements are expected to occur to relax the extra accumulation–depletion anisotropy generated at short times and induce additional particle compression. In the following, we examine the relationship between the static yield strain  $\gamma_p$  and the particle scale dynamical properties.

In Fig. 12(A), we plot the values of  $\gamma_p$  against the persistence strain  $\gamma_d$  associated with elastic collisions for the three volume fractions investigated. The data collapse onto a unique master curve, thereby supporting that  $\gamma_d$  is the elementary clock of the dynamical processes occurring in SPGs [68]. A linear relation is observed at high shear rates where both quantities obey to power-law variations with similar exponents [ $\gamma_p \sim \dot{\gamma}^{0.3}$  from Fig. 12(A) and  $\gamma_d \sim \dot{\gamma}^{0.24}$  from Fig. 4(B) in [68]]. At low shear rates,  $\gamma_p$  approaches the constant value 0.1,

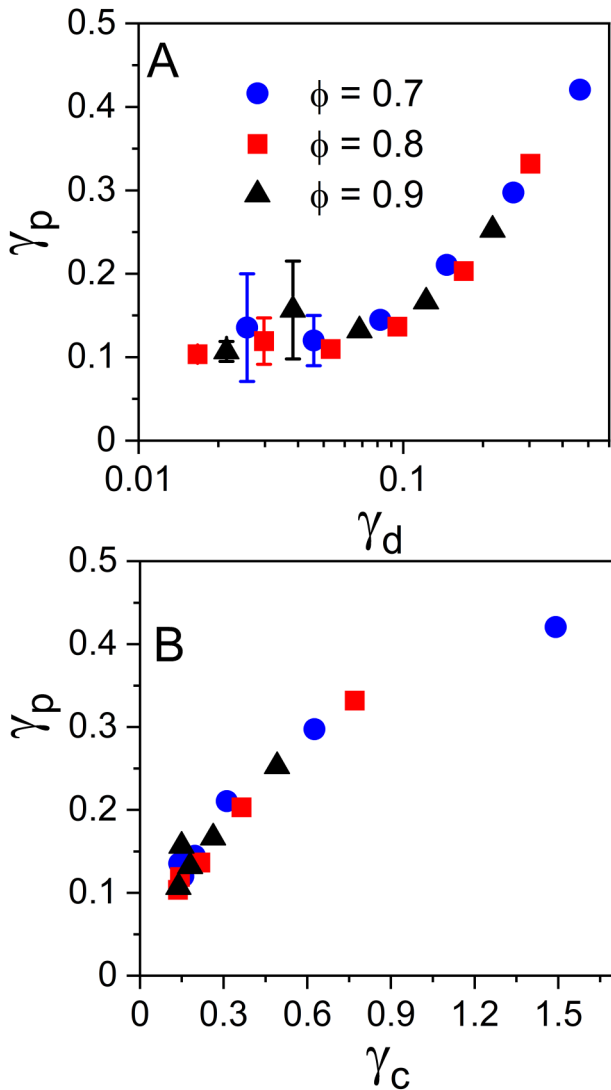


**FIG. 12.** Strain corresponding to the stress overshoot  $\gamma_p$  as a function of (A) the persistence strain of the contact elastic forces during particle collisions,  $\gamma_d$  and (B) residence strain or cage relaxation strain  $\gamma_c$ .

whereas  $\gamma_d \sim \dot{\gamma}$  vary linearly so that the master curve deviates from a linear relationship.

From the results discussed in the microstructure Sec. III B, we anticipate that the stress overshoot marks the onset of large-scale rearrangements so that it must be correlated to the structural relaxation strain that characterizes cage escape. In Fig. 12(B), we plot the static yield strain  $\gamma_p$  as a function of the residence strain  $\gamma_c$ . At low shear rates,  $\gamma_p$  tends to 0.1 and  $\gamma_c$  has a limiting value of 0.13 [68]; as the shear rate increases,  $\gamma_p$  and  $\gamma_c$  increase and collapse onto a master curve for all the studied volume fractions. We note, however, that consistently the values of  $\gamma_p$  are smaller than the cage relaxation strain amplitudes  $\gamma_c$ , which suggests that the stress overshoot might not precisely coincide with the onset of cage escape but instead occurs at lower strain amplitudes.

## V. SUMMARY AND CONCLUSIONS

In this study, we have used particle simulations to study the startup flow of SPGs. Two different macroscopic behaviors have been described. When the applied shear rate is large, the variations of the shear stress, the first and the second normal stress difference as a function of the strain, are characterized by the presence of overshoots, revealing the existence of a static yield point. The overshoots are followed by a decrease of the rheological properties to their steady-state values. At very low shear rates and high volume fractions, the overshoots disappear and the stresses increase monotonically up to their steady-state value. These two regimes can be understood in a qualitative way in terms of the competition between cage rearrangement and flow advection. At high rates, the duration of rearrangements is much larger than the characteristic time of the flow. As a result, the cages deform elastically and store elastic energy until they can no longer sustain the accumulated stress and break, releasing the stored energy. Opposite that, at low shear rates, cages have time to deform so that the stresses are continuously relaxed through local deformation.

The transient stress response is sensitive to the mechanical history of SPGs, as observed experimentally in a variety of materials. The magnitude of the static yield stress increases with the time that SPGs are kept at rest before applying the startup flow. The microstructure is weakly affected. We have shown that the history dependence of the transient rheology of SPGs is associated with the capacity of SPGs to store residual stress and experience physical aging.

The microstructure exhibits dramatic changes, revealing the physical mechanisms at work. The buildup of the stress is associated with structural anisotropy in which particles significantly accumulate along the compression axis and deplete along the extension axis. At high shear rates, where a yield point exists, the pair distribution functions of the SPGs exhibit maximum anisotropy at the stress overshoot, which is relaxed after additional particle compression. At low shear rates, there is a mild compression of the particles, which is reached at very small strain values followed by a monotonic increase of particle accumulation in the compression direction. It is interesting to note that this interplay between accumulation/depletion and particle compression is also central to



the relaxation of SPGs after flow cessation. During stress relaxation, compression is rapidly released by elastic recoil, whereas anisotropy persists over a long period of time and is responsible for residual stresses [64,65]. This shows that the nature of the deformation field to which SPGs are subjected controls the transient responses.

Startup flow simulations and experiments have already been used to investigate the yielding properties of colloidal gels [28,36] and hard-sphere glasses [12–20]. It is, thus, interesting to confront our findings for SPGs to the existing literature. The transient-yielding SPGs and the hard-sphere glasses are characterized by a unique overshoot, which is the signature of repulsive interactions arising from cage elasticity. This distinguishes these materials from colloidal gels, which are characterized by double yielding due to bond rupture and cage breakup at low and high strains, respectively. SPGs and hard-sphere glasses have in common two important features: the absence of stress overshoot at low shear rates and the anisotropy of the pair distribution function between the compression (particle accumulation) and the extension (particle depletion) directions. It is this anisotropy that controls the stress buildup, the maximum anisotropy being in coincidence with the stress overshoot. There is, however, a fundamental difference between soft and hard particle glasses. In hard-sphere glasses, there are no contact interactions and the relaxation occurring after the stress overshoot is due to Brownian motion only. The accumulation in the compression region does not change much, whereas the depletion is partly smoothed out by diffusion [12,19]. In SPGs, the large anisotropy observed at the stress overshoot is relaxed, thanks to an additional compression of particles, with both the compressive and the extension directions being affected. Thus, in SPGs, the capacity of particles to deform elastically plays an important role.

To complete our multiscale understanding of yielding in SPGs, we have found a connection between the static yield strain  $\gamma_p$  and the microstructural relaxation or residence strain  $\gamma_c$  characterizing cage escape and the persistence of the contact interactions  $\gamma_d$ . This shows that the evolution of the macroscopic rheology and the microstructure is connected to the microscopic dynamics, which is known to be controlled by nonaffine particle motion. To draw a bridge with our recent work [68], we speculate that monotonic yielding behavior is associated with the intermittent regime at low applied shear rates where particles have enough time to relax back to a local position before the flow induces a new rearrangement. On the contrary, the yielding behavior at high shear rates can be associated with the regime where particles yield continuously and never find local equilibrium positions.

Several material properties, such as the softness of particles, solvent viscosity, strength of the flow, and packing fraction, affect the magnitude of the overshoot. Here, we have shown that the variations of the static yield strain  $\gamma_p$  and the reduced static yield stress  $\sigma_p/\sigma_y$  with the shear rates computed for different volume fractions collapse onto universal master curves when they are plotted against the nondimensional shear rate of  $\dot{\gamma}\eta_s/G_0$ . The same nondimensional shear rate was used to rationalize the steady flow properties and the microscopic dynamics of SPGs in our previous works [63,66,68,69,80],

confirming that the macroscopic rheology and the microscopic dynamics of SPGs are driven by the competition between flow advection and cage deformation [80]. The variations of the reduced static yield stress  $\sigma_p/\sigma_y$  versus the nondimensional shear rate  $\dot{\gamma}\eta_s/G_0$  are well represented by a Herschel–Bulkley form that is qualitatively similar to that describing the flow curve shown in supplementary material S6 [78]. This similarity expresses that the stress overshoot and the stress at steady state are controlled by a unique physical mechanism, i.e., the anisotropy of the pair distribution function [62].

We have found that the data available from the literature match our master curves, suggesting that our results are relevant for a great variety of systems, including entropic hard-sphere glasses, once the appropriate scaling variables are chosen. These results call for a systematic experimental investigation of the startup flow properties of a variety of jammed suspensions, which will be the topic of a future study.

## ACKNOWLEDGMENTS

F.K. and R.T.B. gratefully acknowledge financial support from the National Science Foundation (MRSEC under Award No. DMR-1720595). B.F.D.D. and M.C. acknowledge financial support from the Innovative Training Network Dodynet (European Program H2020-MSCA-ITN-2017; Grant Agreement No. 765811).

## REFERENCES

- [1] Weeks, E. R., “Introduction to the colloidal glass transition,” *ACS Macro Lett.* **6**, 27–34 (2017).
- [2] Chen, M., “A brief overview of bulk metallic glasses,” *NPG Asia Mater.* **3**, 82–90 (2011).
- [3] Zaccarelli, E., “Colloidal gels: Equilibrium and non-equilibrium routes,” *J. Phys.: Condens. Matter* **19**, 323101 (2007).
- [4] Cohen-Addad, S., and R. Höhler, “Rheology of foams and highly concentrated emulsions,” *Curr. Opin. Colloid Interface Sci.* **19**, 536–548 (2014).
- [5] Coussot, P., “Rheophysics of pastes: A review of microscopic modeling approaches,” *Soft Matter* **3**, 528–540 (2007).
- [6] Bonnecaze, R. T., and M. Cloitre, “Micromechanics of soft particle glasses,” in *High Solid Dispersions* (Springer, Heidelberg, Dordrecht, London and New York, 2010), pp. 117–161.
- [7] Vlassopoulos, D., and M. Cloitre, “Tunable rheology of dense soft deformable colloids,” *Curr. Opin. Colloid Interface Sci.* **19**, 561–574 (2014).
- [8] Bonn, D., M. M. Denn, L. Berthier, T. Divoux, and S. Manneville, “Yield stress materials in soft condensed matter,” *Rev. Mod. Phys.* **89**, 035005 (2017).
- [9] Coussot, P., *Rheometry of Pastes, Suspensions, and Granular Materials Applications in Industry and Environment* (John Wiley & Sons, Hoboken, NJ, 2005).
- [10] Zausch, J., J. Horbach, M. Laurati, S. U. Egelhaaf, J. M. Brader, T. Voigtmann, and M. Fuchs, “From equilibrium to steady state: The transient dynamics of colloidal liquids under shear,” *J. Phys.: Condens. Matter* **20**, 404210 (2008).
- [11] Pham, K., G. Petekidis, D. Vlassopoulos, S. Egelhaaf, W. Poon, and P. Pusey, “Yielding behavior of repulsion- and attraction-dominated colloidal glasses,” *J. Rheol.* **52**, 649–676 (2008).

- [12] Koumakis, N., M. Laurati, S. Egelhaaf, J. Brady, and G. Petekidis, “Yielding of hard-sphere glasses during start-up shear,” *Phys. Rev. Lett.* **108**, 098303 (2012).
- [13] Laurati, M., K. J. Mutch, N. Koumakis, J. Zausch, C. P. Amann, A. B. Schofield, G. Petekidis, J. F. Brady, J. Horbach, M. Fuchs, and S. U. Egelhaaf, “Transient dynamics in dense colloidal suspensions under shear: Shear rate dependence,” *J. Phys.: Condens. Matter* **24**, 464104 (2012).
- [14] Amann, C. P., M. Siebenbürger, M. Krüger, F. Weysser, M. Ballauff, and M. Fuchs, “Overshoots in stress-strain curves: Colloid experiments and schematic mode coupling theory,” *J. Rheol.* **57**, 149–175 (2013).
- [15] Mutch, K. J., M. Laurati, C. P. Amann, M. Fuchs, and S. U. Egelhaaf, “Time-dependent flow in arrested states—Transient behaviour,” *Eur. Phys. J.: Spec. Top.* **222**, 2803–2817 (2013).
- [16] Sentjabrskaja, T., M. Hermes, W. Poon, C. Estrada, R. Castaneda-Priego, S. Egelhaaf, and M. Laurati, “Transient dynamics during stress overshoots in binary colloidal glasses,” *Soft Matter* **10**, 6546–6555 (2014).
- [17] Amann, C. P., D. Denisov, M. T. Dang, B. Struth, P. Schall, and M. Fuchs, “Shear-Induced breaking of cages in colloidal glasses: Scattering experiments and mode coupling theory,” *J. Chem. Phys.* **143**, 034505 (2015).
- [18] Amann, C. P., M. Siebenbürger, M. Ballauff, and M. Fuchs, “Nonlinear rheology of glass-forming colloidal dispersions: Transient stress–strain relations from anisotropic mode coupling theory and thermosensitive microgels,” *J. Phys.: Condens. Matter* **27**, 194121 (2015).
- [19] Koumakis, N., M. Laurati, A. Jacob, K. Mutch, A. Abdellali, A. Schofield, S. Egelhaaf, J. Brady, and G. Petekidis, “Start-up shear of concentrated colloidal hard spheres: Stresses, dynamics, and structure,” *J. Rheol.* **60**, 603–623 (2016).
- [20] Marenne, S., J. F. Morris, D. R. Foss, and J. F. Brady, “Unsteady shear flows of colloidal hard-sphere suspensions by dynamic simulation,” *J. Rheol.* **61**, 477–501 (2017).
- [21] Sentjabrskaja, T., J. Hendricks, A. R. Jacob, G. Petekidis, S. U. Egelhaaf, and M. Laurati, “Binary colloidal glasses under transient stress- and strain-controlled shear,” *J. Rheol.* **62**, 149–159 (2017).
- [22] Jacob, A. R., E. Moghimi, and G. Petekidis, “Rheological signatures of aging in hard sphere colloidal glasses,” *Phys. Fluids* **31**, 087103 (2019).
- [23] Van Aken, B., P. De Hey, and J. Sietsma, “Structural relaxation and plastic flow in amorphous  $\text{La}_{50}\text{Al}_{25}\text{Ni}_{25}$ ,” *Mater. Sci. Eng. A* **278**, 247–254 (2000).
- [24] Johnson, W. L., J. Lu, and M. D. Demetriou, “Deformation and flow in bulk metallic glasses and deeply undercooled glass forming liquids—A self consistent dynamic free volume model,” *Intermetallics* **10**, 1039–1046 (2002).
- [25] Guan, P., M. Chen, and T. Egami, “Stress-temperature scaling for steady-state flow in metallic glasses,” *Phys. Rev. Lett.* **104**, 205701 (2010).
- [26] Mas, R., and A. Magnin, “Rheology of colloidal suspensions: Case of lubricating greases,” *J. Rheol.* **38**, 889–908 (1994).
- [27] Liddel, P. V., and D. V. Boger, “Yield stress measurements with the vane,” *J. Non-Newtonian Fluid Mech.* **63**, 235–261 (1996).
- [28] Koumakis, N., and G. Petekidis, “Two step yielding in attractive colloids: Transition from gels to attractive glasses,” *Soft Matter* **7**, 2456–2470 (2011).
- [29] Chan, H. K., and A. Mohraz, “Two-step yielding and directional strain-induced strengthening in dilute colloidal gels,” *Phys. Rev. E* **85**, 041403 (2012).
- [30] Koumakis, N., P. Ballesta, R. Besseling, W. C. K. Poon, J. F. Brady, and G. Petekidis, “Colloidal gels under shear: Strain rate effects,” *AIP Conf. Proc.* **1518**, 365–371 (2013).
- [31] Colombo, J., and E. Del Gado, “Stress localization, stiffening, and yielding in a model colloidal gel,” *J. Rheol.* **58**, 1089–1116 (2014).
- [32] Park, J. D., and K. H. Ahn, “Structural evolution of colloidal gels at intermediate volume fraction under start-up of shear flow,” *Soft Matter* **9**, 11650–11662 (2013).
- [33] Boromand, A., S. Jamali, and J. M. Maia, “Structural fingerprints of yielding mechanisms in attractive colloidal gels,” *Soft Matter* **13**, 458–473 (2017).
- [34] Park, J. D., K. H. Ahn, and N. J. Wagner, “Structure-rheology relationship for a homogeneous colloidal gel under shear startup,” *J. Rheol.* **61**, 117–137 (2016).
- [35] Johnson, L. C., B. J. Landrum, and R. N. Zia, “Yield of reversible colloidal gels during flow start-up: Release from kinetic arrest,” *Soft Matter* **14**, 5048–5068 (2018).
- [36] Ruiz-Franco, J., N. Gnan, and E. Zaccarelli, “Rheological investigation of gels formed by competing interactions: A numerical study,” *J. Chem. Phys.* **150**, 024905 (2019).
- [37] Letwimolnun, W., B. Vergnes, G. Ausias, and P. J. Carreau, “Stress overshoots of organoclay nanocomposites in transient shear flow,” *J. Non-Newtonian Fluid Mech.* **141**, 167–179 (2007).
- [38] Derec, C., G. Ducoiret, A. Ajdari, and F. Lequeux, “Aging and nonlinear rheology in suspensions of polyethylene oxide-protected silica particles,” *Phys. Rev. E* **67**, 061403 (2003).
- [39] Rogers, S. A., D. Vlassopoulos, and P. Callaghan, “Aging, yielding, and shear banding in soft colloidal glasses,” *Phys. Rev. Lett.* **100**, 128304 (2008).
- [40] Carrier, V., and G. Petekidis, “Nonlinear rheology of colloidal glasses of soft thermosensitive microgel particles,” *J. Rheol.* **53**, 245–273 (2009).
- [41] Zausch, J., and J. Horbach, “The build-up and relaxation of stresses in a glass-forming soft-sphere mixture under shear: A computer simulation study,” *Europhys. Lett.* **88**, 60001 (2009).
- [42] Divoux, T., C. Barentin, and S. Manneville, “Stress overshoot in a simple yield stress fluid: An extensive study combining rheology and velocimetry,” *Soft Matter* **7**, 9335–9349 (2011).
- [43] Koumakis, N., A. Pamvouxoglou, A. S. Poulos, and G. Petekidis, “Direct comparison of the rheology of model hard and soft particle glasses,” *Soft Matter* **8**, 4271–4284 (2012).
- [44] Kurokawa, A., M. Ichihara, and K. Kurita, “Softening of aged fluids in start-up flows of dense suspensions,” *J. Non-Newtonian Fluid Mech.* **217**, 14–22 (2015).
- [45] Dimitriou, C. J., and G. H. McKinley, “A comprehensive constitutive law for waxy crude oil: A thixotropic yield stress fluid,” *Soft Matter* **10**, 6619–6644 (2014).
- [46] Vasisht, V. V., G. Roberts, and E. Del Gado, “Emergence and persistence of flow inhomogeneities in the yielding and fluidization of dense soft solids,” *Phys. Rev. E* **102**, 010604 (2020).
- [47] Vasisht, V. V., and E. Del Gado, “Computational study of transient shear banding in soft jammed solids,” *Phys. Rev. E* **102**, 012603 (2020).
- [48] Partal, P., A. Guerrero, M. Berjano, and C. S. Gallegos, “Transient flow of O/W sucrose palmitate emulsions,” *J. Food Eng.* **41**, 33–41 (1999).
- [49] Ovarlez, G., S. Rodts, A. Ragouilliaux, P. Coussot, J. Goyon, and A. Colin, “Wide-gap Couette flows of dense emulsions: Local concentration measurements, and comparison between macroscopic and local constitutive law measurements through magnetic resonance imaging,” *Phys. Rev. E* **78**, 036307 (2008).
- [50] Khan, S. A., C. A. Schnepfer, and R. C. Armstrong, “Foam rheology: III. Measurement of shear flow properties,” *J. Rheol.* **32**, 69–92 (1988).

- [51] Raufaste, C., S. J. Cox, P. Marmottant, and F. Graner, “Discrete rearranging disordered patterns: Prediction of elastic and plastic behavior, and application to two-dimensional foams,” *Phys. Rev. E* **81**, 031404 (2010).
- [52] Chen, I. J., and D. C. Bogue, “Time-dependent stress in polymer melts and review of viscoelastic theory,” *Trans. Soc. Rheol.* **16**, 59–78 (1972).
- [53] Osaki, K., T. Inoue, and T. Isomura, “Stress overshoot of polymer solutions at high rates of shear,” *J. Polym. Sci. Part B: Polym. Phys.* **38**, 1917–1925 (2000).
- [54] Graham, R. S., A. E. Likhtman, T. C. B. Mcleish, and S. T. Milner, “Microscopic theory of linear, entangled polymer chains under rapid deformation including chain stretch and convective constraint release,” *J. Rheol.* **47**, 1171–1200 (2003).
- [55] Wang, Y., and S.-Q. Wang, “Exploring stress overshoot phenomenon Upon startup deformation of entangled linear polymeric liquids,” *J. Rheol.* **53**, 1389–1401 (2009).
- [56] Snijkers, F., D. Vlassopoulos, G. Ianniruberto, G. Marrucci, H. Lee, J. Yang, and T. Chang, “Double stress overshoot in start-up of simple shear flow of entangled comb polymers,” *ACS Macro Lett.* **2**, 601–604 (2013).
- [57] Cao, J., and A. E. Likhtman, “Simulating startup shear of entangled polymer melts,” *ACS Macro Lett.* **4**, 1376–1381 (2015).
- [58] Jiang, M., G. Wilde, and L. Dai, “Origin of stress overshoot in amorphous solids,” *Mech. Mater.* **81**, 72–83 (2015).
- [59] Wisitsorasak, A., and P. G. Wolyne, “Dynamical theory of shear bands in structural glasses,” *Proc. Natl. Acad. Sci.* **114**, 1287–1292 (2017).
- [60] Ozawa, M., L. Berthier, G. Biroli, A. Rosso, and G. Tarjus, “Random critical point separates brittle and ductile yielding transitions in amorphous materials,” *Proc. Natl. Acad. Sci. U.S.A.* **115**, 6656–6661 (2018).
- [61] Jamali, S., G. H. McKinley, and R. C. Armstrong, “Microstructural rearrangements and their rheological implications in a model thixotropic elastoviscoplastic fluid,” *Phys. Rev. Lett.* **118**, 048003 (2017).
- [62] Seth, J. R., L. Mohan, C. Locatelli-Champagne, M. Cloitre, and R. T. Bonnecaze, “A micromechanical model to predict the flow of soft particle glasses,” *Nat. Mater.* **10**, 838–843 (2011).
- [63] Liu, T., F. Khabaz, R. T. Bonnecaze, and M. Cloitre, “On the universality of the flow properties of soft-particle glasses,” *Soft matter* **14**, 7064–7074 (2018).
- [64] Mohan, L., M. Cloitre, and R. T. Bonnecaze, “Build-up and Two-step relaxation of internal stress in jammed suspensions,” *J. Rheol.* **59**, 63–84 (2014).
- [65] Mohan, L., R. T. Bonnecaze, and M. Cloitre, “Microscopic origin of internal stresses in jammed soft particle suspensions,” *Phys. Rev. Lett.* **111**, 268301 (2013).
- [66] Khabaz, F., T. Liu, M. Cloitre, and R. T. Bonnecaze, “Shear-induced ordering and crystallization of jammed suspensions of soft particles glasses,” *Phys. Rev. Fluids* **2**, 093301 (2017).
- [67] Bonnecaze, R. T., F. Khabaz, L. Mohan, and M. Cloitre, “Excess entropy scaling for soft particle glasses,” *J. Rheol.* **64**, 423–431 (2020).
- [68] Khabaz, F., M. Cloitre, and R. T. Bonnecaze, “Particle dynamics predicts shear rheology of soft particle glasses,” *J. Rheol.* **64**, 459–468 (2020).
- [69] Khabaz, F., M. Cloitre, and R. T. Bonnecaze, “Structural state diagram of concentrated suspensions of jammed soft particles in oscillatory shear flow,” *Phys. Rev. Fluids* **3**, 033301 (2018).
- [70] Liu, K., D. Williams, and B. Briscoe, “The large deformation of a single micro-elastomeric sphere,” *J. Phys. D: Appl. Phys.* **31**, 294–303 (1998).
- [71] Mohan, L., C. Pellet, M. Cloitre, and R. Bonnecaze, “Local mobility and microstructure in periodically sheared soft particle glasses and their connection to macroscopic rheology,” *J. Rheol.* **57**, 1023–1046 (2013).
- [72] Seth, J. R., M. Cloitre, and R. T. Bonnecaze, “Elastic properties of soft particle pastes,” *J. Rheol.* **50**, 353–376 (2006).
- [73] Lubachevsky, B. D., and F. H. Stillinger, “Geometric properties of random disk packings,” *J. Stat. Phys.* **60**, 561–583 (1990).
- [74] Lees, A. W., and S. F. Edwards, “The computer study of transport processes under extreme conditions,” *J. Phys. C* **5**, 1921–1928 (1972).
- [75] Plimpton, S., “Fast parallel algorithms for short-range molecular dynamics,” *J. Comput. Phys.* **117**, 1–19 (1995).
- [76] Larson, R. G., *The Structure and Rheology of Complex Fluids* (Oxford University Press, New York, Oxford), Vol. 150.
- [77] Hanley, H., J. Rainwater, and S. Hess, “Shear-induced angular dependence of the liquid pair correlation function,” *Phys. Rev. A* **36**, 1795–1802 (1987).
- [78] See supplementary material at <https://doi.org/10.1122/8.0000165> for transient behavior during startup flow of the first and second normal stress differences, two-dimensional pair distribution function computed at steady state, spherical harmonics coefficients and , contact number distributions and overlap deformation distributions, shear stress ( $\sigma$ ) as a function of strain in SPGs aged over different waiting times, determination of the dynamic yield stress from the flow curves and collapse of flow curves onto a generic master curve, and experimental values of static yield stress and yield strain available from the literature.
- [79] Cloitre, M., R. Borrega, and L. Leibler, “Rheological aging and rejuvenation in microgel pastes,” *Phys. Rev. Lett.* **85**, 4819–4822 (2000).
- [80] Cloitre, M., R. Borrega, F. Monti, and L. Leibler, “Glassy dynamics and flow properties of soft colloidal pastes,” *Phys. Rev. Lett.* **90**, 068303 (2003).
- [81] Ravindranath, S., and S.-Q. Wang, “Universal scaling characteristics of stress overshoot in startup shear of entangled polymer solutions,” *J. Rheol.* **52**, 681–695 (2008).
- [82] Chatterjee, T., and R. Krishnamoorti, “Steady shear response of carbon nanotube networks dispersed in poly(ethylene oxide),” *Macromolecules* **41**, 5333–5338 (2008).